Article:

Lepadatu, S, Mihai, AP, Claydon, JS et al. (5 more authors) (2012) The increase of the spin-transfer torque threshold current density in coupled vortex domain walls. Journal of Physics: Condensed Matter, 24 (2). 024210 - ? . ISSN 0953-8984

https://doi.org/10.1088/0953-8984/24/2/024210

Increase of spin-transfer torque threshold current density in coupled vortex domain walls

S. Lepadatu[1], A.P. Mihai[1], J.S. Claydon[1], F. Maccherozzi[2], S.S. Dhesi[2], C.J. Kinane[3], S. Langridge[3] and C.H. Marrows[1]

[1]School of Physics and Astronomy, E.C. Stoner Laboratory, University of Leeds, Leeds LS2 9JT, United Kingdom

[2]Diamond Light Source, Chilton, Didcot OX11 0DE, United Kingdom

[3]ISIS, Rutherford Appleton Laboratory, Chilton, Didcot OX11 0QX, United Kingdom

Abstract:

We have studied the dependence on domain wall structure of the spin-transfer torque current density threshold for the onset of wall motion in curved, Gd-doped $Ni_{80}Fe_{20}$ nanowires with no artificial pinning potentials. For single vortex domain walls, both for 10% and 1% Gd doping concentrations, the threshold current density is inversely proportional to the wire width and significantly lower compared to the threshold current density measured for transverse domain walls. On the other hand for high Gd concentrations and large wire widths, double vortex domain walls are formed which require an increase in the threshold current density compared to single vortex domain walls at the same wire width. We suggest that this is due to the coupling of the vortex cores, which are of opposite chirality, and hence will be acted on by opposing forces arising through the spin-transfer torque effect.

Current-induced domain wall motion is being actively pursued as a basis for the operation of magnetic memory devices such as race-track memory [1] and magnetic logic [2]. The main difficulty stems from the large current densities required for the operation of such devices, which results in rapid degradation and eventual failure due to electromigration and accumulated damage from heating. As the domain wall is initially at rest the local pinning must be overcome in order for current-induced domain wall motion to be initiated. Two types of local pinning may be distinguished, intrinsic pinning arising from material properties alone such as hard axis anisotropy [3] and extrinsic pinning due to artificially created pinning potentials [4,5] or defects such as edge roughness [6,7]. Methods of reducing the threshold current density have been investigated, including resonant excitation of domain walls [8] in wires with no pinning potentials [9] as well as wires with artificial pinning potentials [10,11], and modification of material parameters by addition of dopant concentrations [12].

We have previously studied the threshold current density required for domain wall depinning from artificial pinning potentials, where the extrinsic pinning dominates the intrinsic pinning [4]. Here we study the opposite case where the sources of extrinsic pinning are minimized in order to characterize the dependence of the intrinsic pinning on domain wall structure and material parameters. This problem is addressed here for double vortex structures: coupled pairs of vortex domain walls where the motion of the vortex cores is interdependent.

Smoothly curved L-shaped nanowires have been fabricated on highly resistive Si/SiO_2 substrates using electron beam lithography with varying width from 2 μm down to 200 nm. The wires have pointed ends to suppress domain wall formation at either end. Gd doped $Ni_{80}Fe_{20}$ (Py) was sputtered from stoichiometric targets with 1 % and 10 % Gd concentration, 10 nm thick, and the wires were obtained using lift-off. A second electron beam lithography step was used to define the Ti (10 nm) / Au (50 nm) electrical leads as shown in the inset to Fig. 1(a), whilst the main contact pads were defined using optical lithography and sputtering of Ti (10 nm) / Au (120 nm). The current injection and voltage measurement configuration is also shown in the inset to Fig. 1(a). The current injection pads were connected to a voltage pulser using impedance matched probes, whilst the wire resistance was measured using a lock-in amplifier method. External magnetic fields were applied in the direction indicated in Fig. 1(b), slightly offset from the direction that bisects the wire corner.

A typical magneto-resistance (MR) response of a curved wire is shown in Fig. 1(a) with the main magnetization configuration states labelled A through D on the positive-going field sweep (symmetrically equivalent states are to be found on the negative-going sweep). Micromagnetic simulations of these states, obtained using the OOMMF code [13], are shown in Fig. 1(b). In state A the magnetization in the wire is almost saturated by a large negative field across its width in the region between the voltage probes, resulting in a minimum resistance due to the anisotropic MR effect (AMR). Relaxing the magnetic field to zero results in domain wall formation in the curved section of the wire at zero field, state B, owing to the shape anisotropy of the wire which forces the magnetization to align along the length of the wire in opposite direction on either side of the curve. The resistance has risen due to AMR, as most of the wire—all but for the domain wall—now has its magnetization lying parallel to the current path. The application of a positive magnetic field switches the wire into a single domain, state C, with the domain wall travelling through the right-hand side section of the wire under the action of the magnetic field. State C' is a snapshot of this process occurring. This results in a small but sharp increase in resistance due to the AMR effect as the wall is expelled, just before state C is achieved. A slight deviation of 5º from the perpendicular direction of the magnetic fields has been used, as shown in Fig. 1(a), to result in reproducible domain wall motion towards the right. A further sharp increase in resistance is observed just prior to obtaining state D, as the magnetic field is increased resulting in coherent magnetization rotation of the left section of the wire. This aligns the magnetic moments of that section more closely to the wire axis, and thus more parallel to the current flow, due to shape anisotropy, resulting in an overall increase in resistance due to AMR. For a large enough magnetic field the wire is saturated again and the resistance drops to the same value as for state A.

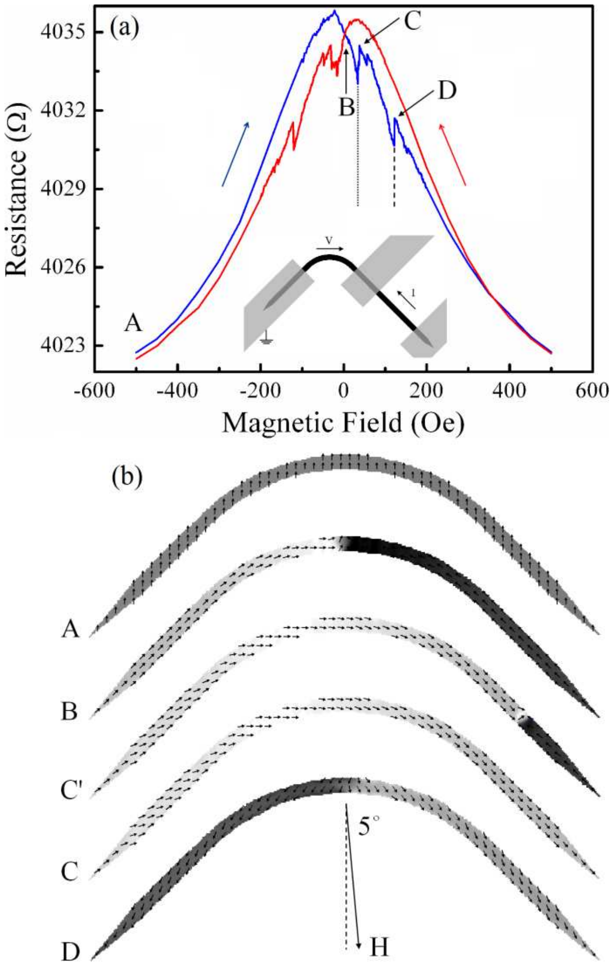

Figure 1 – (colour online) (a) Magnetoresistance for a curved wire (200 nm wide, $Py_{99}Gd_1$) and (b) micromagnetic simulations showing the magnetization switching steps. In the inset of (a) the electrical contact configuration is shown. State A is at saturation, state B at zero field with a domain wall formed, state C is the single domain state after the domain wall is expelled out of the right arm, with C’ occurring during this process, and state D is obtained after coherent rotation of magnetization in the left arm. The dotted and dashed lines indicate the switching fields for domain wall motion and coherent rotation respectively, which may easily be determined by AMR measurements.

The variation in the two switching fields – domain wall motion for right arm switching and coherent magnetization rotation for left arm switching – is shown in Fig. 2 as a function of arm width for both Gd-doping concentrations. As expected, due to the decrease in arm width, both the domain wall motion and magnetization rotation switching fields increase [14]. On the other hand the switching fields are significantly reduced for the larger Gd concentration, owing to the reduction in net magnetic moments with Gd doping, which we have measured previously, as the switching field is dominated by the shape anisotropy [15], which is in turn proportional to the square of the magnetization.

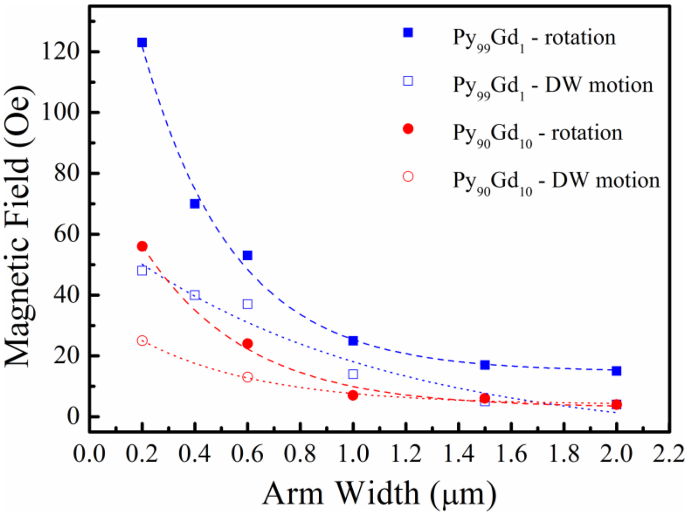

Figure 2 – (colour online) Switching fields measured by AMR as a function of arm width and Gd concentration. The lines are guides for the eye.

The remanent domain wall structure (state B) was investigated by means of x-ray magnetic circular dichroism photo-emission electron microscopy (PEEM) imaging with the I06 beamline at the Diamond Light Source synchrotron. Imaging was carried out at near zero field (less than 1 Oe), after saturation in 700 Oe. Circularly-polarized x-ray photons with energies corresponding to the Fe L_3 and L_2

absorption edges have been used. By obtaining two PEEM images with the x-ray beam angle with respect to the sample in orthogonal directions a vector map of the magnetization is obtained, as explained previously [10]. Images of the domain wall structures as a function of wire width and Gd concentration are shown in Fig. 3. For the 200 nm wire width we find transverse domain walls are formed, in agreement with previous calculations of the domain wall phase diagram in Py [16]. For the wider wires we observe single vortex domain wall formation, with the exception of the 1.5 μm and 2 μm wide $Py_{90}Gd_{10}$ wires for which we observe a remarkable double vortex domain wall structure. The double vortex domain wall consists of two coupled vortex structures with opposite chiralities as shown in Fig. 3(c). As we have previously found, Gd doping of permalloy increases the out-of-plane anisotropy [15]. This results in lower energy cost of supporting a vortex core, which may explain the formation of double vortex domain walls for the larger Gd concentration.

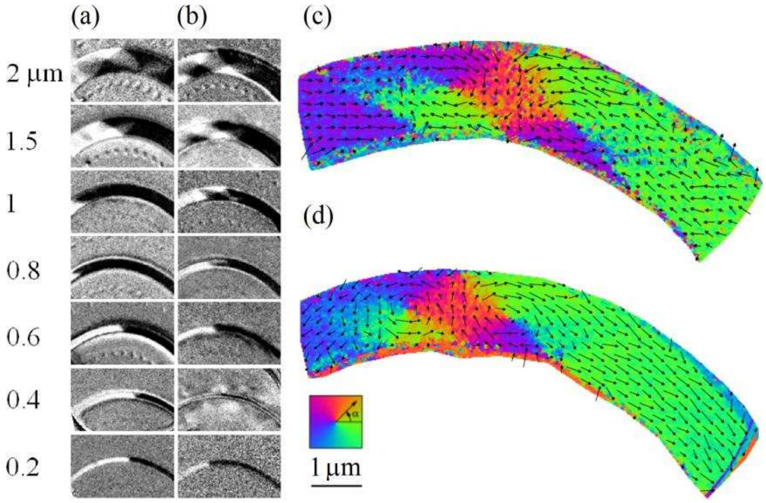

Figure 3 – (colour online) PEEM images of domain wall structure as a function of wire width and Gd concentration, (a) 1 % Gd concentration and (b) 10 % Gd concentration with the exception of the 200 nm wide wire which has 2.5 % Gd concentration. (c) and (d) PEEM vector maps of 2 μm and 1.5 μm wide $Py_{90}Gd_{10}$ wires respectively, showing the detail of the double vortex wall structures.

We next investigate the effect of domain wall structure and wire width on the threshold current density for current-induced domain wall motion. For these measurements we first form a domain wall between the voltage measurement leads by saturating with a large magnetic field (-700 Oe) and then setting the field to zero. Following domain wall formation a series of voltage pulses (~2000) of controlled height and fixed duration of 70 ns was injected between the outer current injection leads resulting in electron flow direction towards the right injection lead – see inset to Fig. 1(a). A large number of pulses with a short duration was chosen so as to minimize the risk of wire damage over repeated measurements due to excessive heating, whilst still having a sufficiently long time to completely remove the domain wall. We also performed measurements with longer current pulses (50 µs) and obtained the same values of threshold current. Following voltage pulse injection the depinning of domain walls from between voltage measurement leads was tested by measuring the MR response of the wires on returning to the negative starting field, as shown in Fig. 4. For small voltage pulse heights, where the domain wall remains between the voltage measurement leads, a smooth decrease in resistance is measured with increasing magnetic field intensity as the wire gradually reverses from state B to state A. For large enough voltage pulse heights to remove the domain wall from between the voltage measurement leads, generating state C, (in addition to a small initial increase in resistance due to the removal of the AMR contribution of the domain wall) a switching event is measured as the wire switches into state D at the magnetic field corresponding to magnetization rotation in the right arm, as shown in Fig. 4. We use the latter method to detect removal of the domain wall as it is more reliable than simply measuring the resistance at zero field following voltage pulse injection.

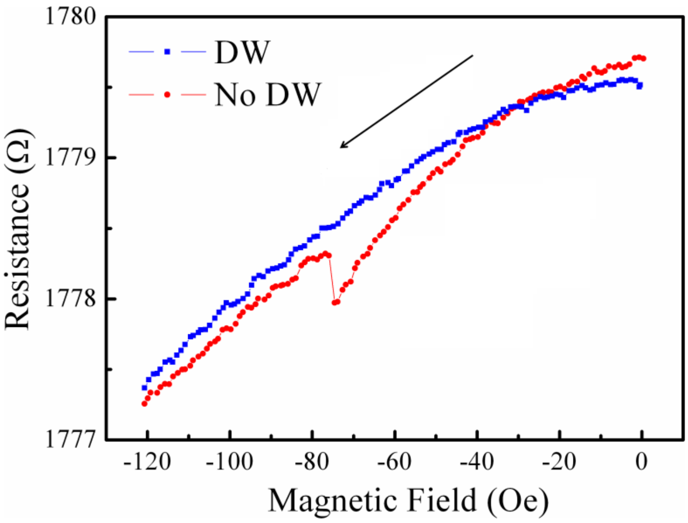

Figure 4 – (colour online) Domain wall movement detection method. If the DW remains in the corner of the wire it can smoothly return to a saturated state, whilst if it was ejected by the current pulse a new wall has to be created and annihilated to reach saturation, leading to a step-like feature in the magnetoresistance response.

The results are summarised in Fig. 5, showing the variation of threshold current density with arm width for the two different Gd concentrations. We group the DWs by their topology, as determined from the PEEM imaging. The threshold current densities for transverse walls are larger compared to those for vortex walls in agreement with previous reported work [17]. For vortex domain walls the threshold current density decreases as the arm width is increased for both $Py_{99}Gd_1$ and $Py_{90}Gd_{10}$. In the absence of pinning potentials, for large domain walls in the purely adiabatic limit where the spin transfer mechanism dominates as is the case here, i.e. domain wall width $\lambda >> \lambda_F$, where λ_F is the Fermi wavelength, the threshold current density j_{TH} is determined by the hard axis anisotropy K according to [3]

$$j_{TH} = \frac{eS^2}{a^3\hbar} K\lambda, \qquad \text{(Eq. 1)}$$

where a is the lattice constant and S the magnitude of the localized spin. For transverse domain walls the threshold current is set by the hard axis in-plane anisotropy with the edge roughness contributing a further increase of the threshold current due to extra pinning [17]. For the 200 nm wide $Py_{99}Gd_1$ and $Py_{90}Gd_{10}$ wires, the contribution from edge roughness pinning is expected to be equal. Since for a planar wire the hard axis anisotropy is set by the shape anisotropy, the reduction in net magnetic moment for $Py_{90}Gd_{10}$ compared to $Py_{99}Gd_1$ [15] explains the lower threshold current measured for $Py_{90}Gd_{10}$.

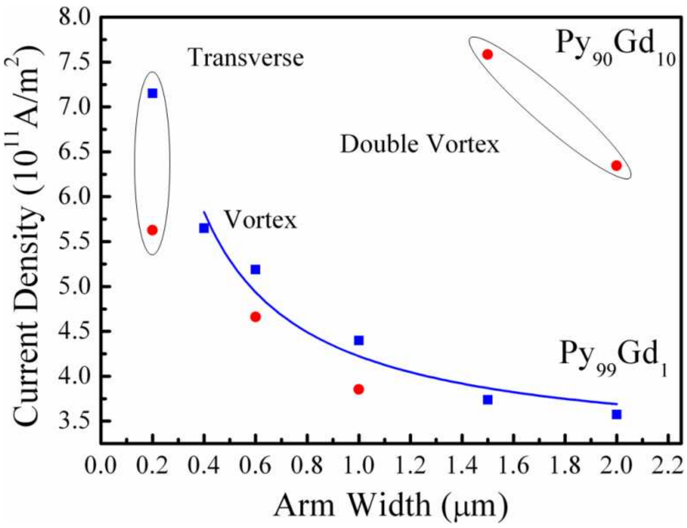

Figure 5 – (colour online) Threshold current density as a function of arm width and Gd concentration. Circles are for $Py_{90}Gd_{10}$ and squares for $Py_{99}Gd_1$. A fit using Eq. 2 to the vortex domain walls for $Py_{99}Gd_1$ is also shown as the solid line.

For vortex domain walls, since the vortex core magnetization is perpendicular to the sample plane, the threshold current is set by the out-of-plane hard axis anisotropy [3]. We have previously measured an increase in the out-of-plane anisotropy field with Gd doping [15] leading to a decrease in the energy required to support a vortex core, resulting in lower threshold currents for $Py_{90}Gd_{10}$ vortex domain walls compared to $Py_{99}Gd_1$. As shown by Heyne et al. [18] the threshold current density required for continuous motion of a vortex wall is connected to the energy cost of creating a vortex-antivortex pair at the wire edges. Since $\alpha \neq \beta$, where α is the Gilbert damping and β is the non-adiabaticity parameter, as the vortex domain wall is displaced the vortex core attains a transverse displacement dependent on its polarity. As the vortex core reaches the wire edge a vortex-antivortex pair is nucleated with opposite polarity and the antivortex annihilates with the original vortex. This process leaves behind a single vortex core with reversed polarity which is now able to move towards the opposite wire edge as the whole vortex domain wall is displaced along the wire [18]. The energy cost of creating the vortex-antivortex pair depends on the out-of-plane anisotropy and results in an inverse dependence of threshold current density on wire width W according to [18]

$$j_{TH} = j_W + j_0 = \frac{2e}{\pi\hbar}\frac{d_v^2}{a^3}\frac{K}{W} + j_0, \qquad \text{(Eq. 2)}$$

where d_v is the vortex core size (~10 nm). A further contribution to the threshold current density, termed j_0, must be included in order to reproduce the results shown in Fig. 5 for vortex domain walls, as the measured threshold current densities do not approach zero as W increases. A fit using Eq. 2 to the results for vortex domain walls in $Py_{99}Gd_1$ is also shown in Fig. 5, where we obtain the value $j_0 = 3.2\times10^{11}$ A/m^2.

There are not enough data points in any one group to do a quantitative fit to the data for the $Py_{99}Gd_{10}$ samples, but the value of j_0 does not seem to be very different for these nanowires from the overall trend in the data. The origin of this offset threshold current density is most likely to be the weak pinning resulting from edge roughness and magnetic non-uniformity which cannot be completely eliminated in real systems. Note that we obtain the same values of threshold currents when repeating the measurements with single voltage pulses of much longer duration of 70 μs, as the critical point which needs to be overcome to sustain continuous domain wall motion is the creation of the vortex-antivortex pair which requires the largest current density. Thus for the start-stop measurements using the shorter 70 ns pulses the domain wall will also be completely removed from between the voltage measurement pads provided the initial current density is large enough to overcome the threshold required for vortex-antivortex pair creation. We also note that the shorter 70 ns pulse duration is long enough to avoid the oscillatory dynamical effects observed at shorter pulse durations. [9]

We now analyse the case of the double vortex domain walls present in the 1.5 and 2 μm wide $Py_{90}Gd_{10}$ wires. In contrast to the $Py_{99}Gd_1$ wires, larger threshold currents are measured for the double vortex domain walls, roughly two times larger, as shown in Fig. 5. This stands in contrast to the dependence of domain wall propagation fields on wire width and Gd doping in Fig. 2, showing that extrinsic pinning due to edge roughness and magnetic non-uniformity cannot alone explain the results shown in Fig. 5. On the other hand, the mechanism of vortex-antivortex pair creation may be used to understand the larger threshold currents required to fully displace the double vortex domain walls. As for the single vortex domain walls, the vortex cores undergo a transverse displacement towards the wire edges and reverse polarity following creation of vortex-antivortex pairs and annihilation with the original vortex cores. For the double vortex wall, effectively a system of two coupled vortices with opposite chiralities, the energy required to create two vortex-antivortex pairs is increased by at least a factor of two, resulting in an increase of the threshold current density. Note that we expect the threshold current density for two vortex domain walls sufficiently far apart to revert back to Eq. 2 as the motion of the two vortex cores becomes independent.

Finally we discuss the effect of non-adiabaticity. The non-adiabatic spin-transfer torque is introduced into the Landau-Lifshitz-Gilbert equation as a second order modification to the purely adiabatic spin-transfer torque, and is directly proportional to the spin-flip scattering rate [6]. For steady-state domain wall motion, below Walker breakdown the domain wall velocity, v, is given by $\mathrm{v} = \beta \mathrm{u} / \alpha$ where $\mathrm{u} = \mathrm{JPg}\mu_{\mathrm{B}} / 2\mathrm{eM}_{\mathrm{S}}$ with P being the current spin-polarization, J the current density and $\mathrm{M_S}$ the saturation magnetization. Thus for a perfect wire and $\beta > 0$, steady domain wall movement may be sustained at arbitrarily small current densities. Thiaville et al. [6] have shown that if imperfections are introduced, a threshold current density is required for steady domain wall movement, which decreases as β is increased. We have previously shown that Gd doping of Py results in increased values of β [12] which in the present case should result in decreased threshold current density due to extrinsic pinning, namely $\mathrm{j_0}$. On the other hand the increase in β does not affect the threshold current density arising due to intrinsic pinning, namely $\mathrm{j_W}$.

In conclusion, by varying the wire width and Gd doping of Py we have studied the dependence of threshold current density on domain wall structure and material parameters. In all cases the threshold current density may be separated in two contributions, one arising from intrinsic pinning due to the hard axis anisotropy and the other from extrinsic pinning due to pinning potentials resulting from imperfections. The threshold current density arising from intrinsic pinning is inversely dependent on wire width for vortex domain walls and is more than doubled for systems of two coupled vortex walls. On the other hand the threshold current density arising from extrinsic pinning is independent of wire width and inversely proportional to the non-adiabaticity parameter.

This research was supported by the UK EPSRC. We are grateful to the Diamond Light Source for the provision of beamtime, and to Gen Tatara for useful discussions.

References

[1] S.S.P. Parkin, M. Hayashi, L. Thomas, Science **320**, 190, (2008)

[2] P. Xu, K. Xia, C. Gu, L. Tang, H. Yang, J. Li, Nature Nanotech. **3**, 97 (2008)

[3] G. Tatara, H. Kohno, Phys. Rev. Lett. **92**, 086601 (2004)

[4] S. Lepadatu, A. Vanhaverbeke, D. Atkinson, R. Allenspach, C.H. Marrows, Phys. Rev. Lett. **102**, 127203 (2009)

[5] D. Bedau, M. Kläui, S. Krzyk, U. Rüdiger, G. Faini, L. Vila, Phys. Rev. Lett. **99**, 146601 (2007)

[6] A. Thiaville, Y. Nakatani, J. Miltat and Y. Suzuki, Europhys. Lett. **69**, 990 (2005)

[7] M. Kläui, P.-O. Jubert, R. Allenspach, A. Bischof, J.A.C. Bland, G. Faini, U. Rüdiger, C.A.F. Vaz, L. Vila, C. Vouille, Phys. Rev. Lett. **95**, 026601 (2005)

[8] E. Saitoh, H. Miyajima, T. Yamaoka, G. Tatara, Nature (London) **432**, 203 (2004)

[9] L. Thomas, M. Hayashi, X. Jiang, R. Moriya, C. Rettner, S.P. Parkin, Nature (London) **443**, 197 (2006)

[10] S. Lepadatu, J.S. Claydon, C.J. Kinane, T.R. Charlton, S. Langridge, A. Potenza, S.S. Dhesi, P.S. Keatley, R.J. Hicken, B.J. Hickey, C.H. Marrows, Phys. Rev. B **81**, 060402 (2010)

[11] R. Moriya, L. Thomas, M. Hayashi, Y.B. Bazaliy, C. Rettner, S.P. Parkin, Nat. Phys. **936** (2008)

[12] S. Lepadatu, J.S. Claydon, D. Ciudad, A. Naylor, C.J. Kinane, S. Langridge, S.S. Dhesi, C.H. Marrows, Appl. Phys. Exp. **3**, 083002 (2010)

[13] M.J. Donahue and D.G. Porter, OOMMF User's Guide, Version 1.0, Interagency Report NISTIR 6376, National Institute of Standards and Technology, Gaithersburg, MD (Sept 1999).

[14] L.K. Bogart, D.S. Eastwood, D. Atkinson, J. Appl. Phys. **104**, 033904 (2008)

[15] S. Lepadatu, J.S. Claydon, D. Ciudad, C.J. Kinane, S. Langridge, S.S. Dhesi, C.H. Marrows, Appl. Phys. Lett. **97**, 072507 (2010)

[16] Y. Nakatani, A. Thiaville, J. Miltat, J. Magn. Magn. Mater. **290**, 750 (2005)

[17] L. Heyne, M. Kläui, D. Backes, T.A. Moore, S. Krzyk, U. Rüdiger, L.J. Heyderman, A.F. Rodriguez, F. Nolting, T.O. Mentes, M.Á. Niño, A. Locatelli, K. Kirsch and R. Mattheis, Phys. Rev. Lett. **100**, 066693 (2008)

[18] L. Heyne, J. Rhensius, Y.-J. Cho, D. Bedau, S. Krzyk, C. Dette, H.S. Körner, J. Fischer, M. Laufenberg, D. Backes, L.J. Heyderman, L. Joly, F. Nolting, G. Tatara, H. Kohno, S. Seo, U. Rüdiger, M. Kläui, Phys. Rev. B **80**, 184405 (2009)